Field-Aligned Isotropic Surface Remeshing

Xingyi Du[1],   Xiaohan Liu[2,3],   Dong-Ming Yan[2],   Caigui Jiang[4],   Juntao Ye[2],   Hui Zhang[1]

[1]Software School, Tsinghua Univ.   [2]NLPR, Institute of Automation, Chinese Academy of Sciences
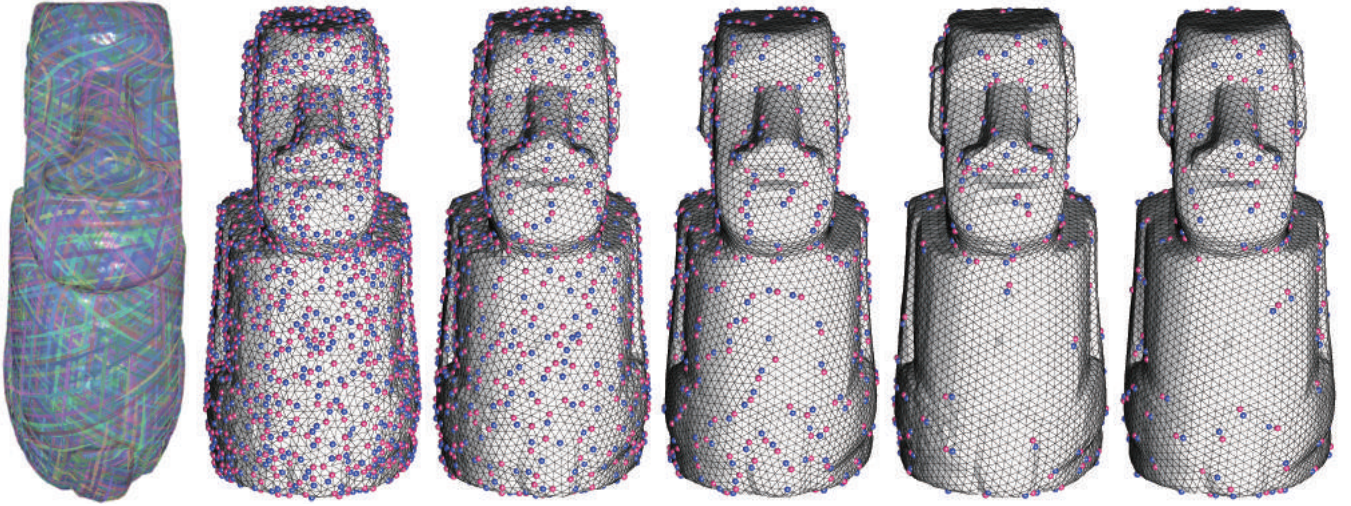[3]Univ. of Chinese Academy of Sciences   [4]Max Planck Institute for Informatics

Figure 1: *Comparison of our approach with the representative state-of-the-art approaches. From left to right: a 6-RoSy field defining the Moai surface, remeshing results of blue-noise sampling [YW13], discrete mesh optimization [DVBB13], centroidal Voronoi Tessellation [YLL*09], instant field-aligned meshing [JTPS15], and our result. The irregular vertices of the remeshes are colored using blue (degree < 6) and pink (degree > 6) colors. The mesh quality is given in Table 2. Our remeshing is both isotropic and field aligned, i.e., it has only a few irregular vertices similar to [JTPS15] while keeping the mesh quality as high as a CVT-based method [YLL*09].*

Abstract

We present a novel isotropic surface remeshing algorithm that automatically aligns the mesh edges with an underlying directional field. The alignment is achieved by minimizing an energy function that combines both centroidal Voronoi tessellation and the penalty enforced by a six-way rotational symmetry (6-RoSy) field. The CVT term ensures the uniform distribution of the vertices and the high remeshing quality, while the field constraint enforces the directional alignment of the edges. Experimental results show that the proposed approach has the advantages of both isotropic remeshing and field-aligned remeshing. We demonstrate that our algorithm is superior to the representative state-of-the-art approaches in various aspects.

Categories and Subject Descriptors (according to ACM CCS): I.3.6 [Computer Graphics]: Methodology and Techniques—Remeshing

1. Introduction

Triangle meshes are commonly used in computer graphics and many other applications. Nowadays, there are multiple ways to acquire meshes with high accuracy, e.g., using a 3D laser scanner, a RGBD camera, dense reconstruction from multi-view stereo im-

ages, isosurface contouring, and so on. It is difficult to use these acquired raw meshes directly in downstream applications, since they usually contain redundant data and the mesh quality is quite low. A remeshing step is necessary to improve the mesh quality while keeping the original geometry as much as possible.

There are various application-oriented criteria for surface remeshing. In this paper, we shall focus on the most popular isotropic remeshing. All the remeshing algorithms should follow three common criteria: simplicity, low approximation error, and high mesh quality [AUGA08]. However, these goals usually conflict with each other, e.g., highly regular meshes always have more distorted triangles, while meshes with high triangle quality always contain more singular vertices (e.g., remeshing with *Centroical Voronoi Tessellation* (CVT) [DFG99]). Fig. 1 illustrates this fact.

Directional fields can be naturally defined on surfaces, and are commonly used for quadrilateral remeshing. Typical directional fields include the principal curvature directions [BLP*13], conjugate direction fields [LXW*11], or harmonic fields [DKG05]. The edges of quad meshes are naturally aligned with the underlying fields via a global parameterization. However, this is not true for isotropic remeshing, where enforcing the field-alignment property is somehow ignored, i.e., one disadvantage of isotropic remeshing is that it cannot preserve the directional features of the input mesh due to its isotropic nature, e.g., the cylindrical blending regions (e.g., the body of the Moai model shown in Fig. 1). The recent work of Jakob et al. [JTPS15] propose an algorithm for generating isotropic triangle meshes which simultaneously align to a predefined underlying directional field, called *Instant Field-aligned Meshing* (IFM). Although they are able to generate highly regular triangle meshes with fewer number of singular vertices, it is unavoidable to sacrifice the triangle quality due to distortion.

In this paper, we propose a novel approach for field-aligned isotropic remeshing. We use 6-RoSy fields to represent the target orientation of the output mesh edges, since 6-RoSy fields are the most natural guidance fields for triangle meshes. However, our formulation can easily be generalized to other fields. Our method is built on top of the remeshing framework based on CVT and the *Restricted Voronoi Diagram* (RVD) on surfaces [YLL*09]. We add a novel penalty term to the CVT energy function, which enforces the mesh edges to align to the underlying field. The presented approach, called FCVT, preserves the advantages of CVT, as well as the directional features of the field. Furthermore, we incorporate valence optimization operations in our remeshing framework, which further improve the mesh quality. The main contributions of this paper include:

- A novel formulation for field-aligned isotropic remeshing.
- A simple interpolation method for 6-RoSy fields.
- A comprehensive comparison with recent representative state-of-the-art approaches.

2. Related Works

Isotropic surface remeshing has been extensively studied in literature. Representative approaches include particle reactions [Tur92, Mey07, BW10, AGY*17], Delaunay insertion [Che93, Boi05, CDS12], discrete local operators [HDD*93, BK04, DVB-B13, HYB*17], randomized sampling [YW13, GYJZ15, ERA*16], and variational approaches, e.g., *Centroidal Voronoi Tessellation* (CVT) [DFG99], *Optimal Delaunay Triangulation* (ODT) [Che04], and their variations [CCW12, Ren15]. Among all these techniques, the CVT-based approach gains more attention due to its elegant the-

oretical background and the ability to generate high-quality meshes. The CVT-based approaches can further be classified into several categories according to how the Voronoi diagram on surfaces computed, e.g., mesh parameterization [AMD02, AVDI03], discrete clustering [VCP08], the restricted Voronoi diagram [YLL*09, Y-BZW14, YW16], and the geodesic Voronoi diagram [SSG03, FZ08, WYL*15, LXY*16]. The readers are referred to the comprehensive survey by Alliez et al. [AUGA08] and the textbook by Botsch et al. [BKP*10] for more details of the recent advantages of surface remeshing.

Although the above discussed isotropic algorithms are able to generate high-quality meshes efficiently, they cannot produce good results near highly non-isotropic regions, e.g., the cylindrical blending areas of CAD models. The anisotropic remeshing algorithms aim to handle such cases, but they tend to introduce many thin and long triangles [LB12, ZGW*13, FLSG14, BSTY15].

A natural way to align mesh edges with the principal direction is to define a directional field on the input domain, and then extract the new mesh from the field w.r.t. a user specified precision. The most well-known directional field is the min/max principal curvature directions, which is commonly used for quadrilateral remeshing [BLP*13], or quad-dominant mixed remeshing [ACSD*03, L-L10].

There exists several approaches that extract isotropic triangle meshes from 6-RoSy directional fields. For example, Lai et al. [LJX*10] propose a method to generate RoSy field that allows users to fully control the field topology and interactively modify it. Huang et al. [HZP*11] use 6-RoSy field and density field to generate 3 scalar fields on the input surface and construct meshes by extracting the isolines of the scalar fields. Nieser et al. [NPPZ11] use a 6-Rosy field-guided global paremeterization to generate triangular and hexagonal meshes. The field is aligned to one of the principal directions which is automatically selected by the algorithm. However, the input meshes have to be cut into disk-like topology for parameterization, and then be stitched back to finalize the remeshing process. More recently, Jakob et al. [JTPS15] propose the extrinsic smooth directional field, which better aligns to underlying surface features than the previous "intrinsic smooth" fields. The field is generated by multi-resolution Gauss-Seidel method, which is robust and efficient. Unfortanately, the mesh quality of this type of approaches still suffers from the distortion caused by tracing the field.

3. Field-aligned CVT Formulation

In this paper, we propose a novel approach for field-aligned isotropic remeshing algorithm, which is based on the well-studied CVT and field meshing techniques, where field alignment is enforced by a penalty term added to the CVT energy. Given an input mesh surface $\mathcal{M}$, and a set of sampled points $\mathbf{X}$ on $\mathcal{M}$, we propose the following energy function:

$$E_{tot} = E_{CVT} + \lambda E_{field},$$

where $\lambda \geq 0$ is a user-specified parameter, which balances the relative importance of the directional alignment requirement. In the rest of this section, we first introduce the basic concepts of CVT,
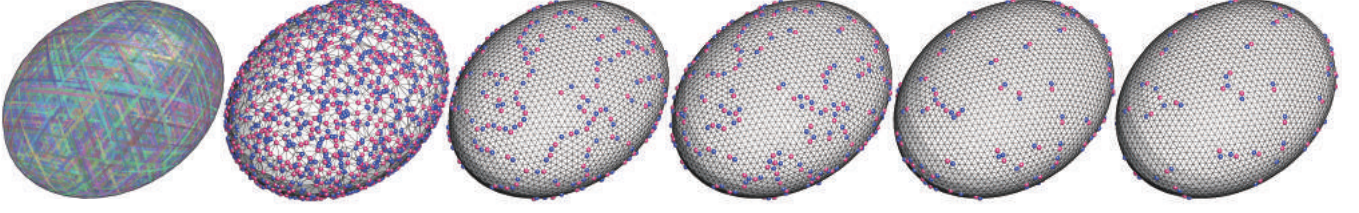
Figure 2: *From left to right are: the field, initial mesh, result of CVT, result of 10 iterations, 50 iterations and final result.*

RoSy field, extrinsic smoothness of a given field, and then discuss the details of the proposed field alignment term.

3.1. Centroidal Voronoi tessellation

The CVT energy term is defined as

$$E_{CVT}(\mathbf{X}) = \sum_{i=1}^{n} \int_{\Omega_{i|\mathcal{M}}} \rho(\mathbf{x}) \|\mathbf{x} - \mathbf{x}_i\|^2 \, d\sigma, \quad (1)$$

where $\Omega_{i|\mathcal{M}}$ is the *Restricted Voronoi Cell* (RVC) [YLL*09] of the point $\mathbf{x}_i$, defined as the intersection of the Voronoi cell Ω_i of $\mathbf{x}_i$ and the mesh surface $\mathcal{M}$; $\rho(\mathbf{x}) > 0$ is a user-defined density function. When ρ is constant, we get a uniform CVT. The dual of the restricted Voronoi diagram is called *Restricted Delaunay Triangulation* (RDT), which is actually a remeshing of $\mathcal{M}$.

3.2. Rotational symmetry field

The RoSy field is commonly used in parameterization and quadrilateral mesh generation. *N*-way rotational symmetry field, or *N*-RoSy field over a surface, defines *N* distinct directions at every surface point $\mathbf{x}$, where all the directions lie in the tangent plane at $\mathbf{x}$ and each pair of adjacent directions form an angle of $\frac{2\pi}{N}$. Here, we use 6-RoSy field as the target orientation for mesh edges since it naturally implies the symmetry of triangular mesh. For more details of directional field, please refer to the recent survey papers [dGDT16, Zha16, VCD*16].

3.3. Extrinsic smoothness property

The Extrinsic smoothness proposed in [JTPS15] measures the smoothness of a given RoSy field by calculating difference between proximate field directions directly in 3D space. Jakob et al. [JTPS15] experimentally demonstrates that the extrinsic smoothness leads to better alignment to sharp features of the input surface. A theoretical analysis of extrinsic smoothness is also provided by Huang and Ju [HJ16a].

Similar to field smoothing, Our field-alignment problem also aims at minimizing the difference between the edge direction and the direction of local field. Inspired by the extrinsic smoothness, we measure the difference directly in 3D space, which results in a simple yet powerful formulation of the field alignment constraint.

3.4. Field alignment

The field alignment term is formulated as the weighted sum of the directional distance *D* of all mesh edges in the restricted Delaunay

triangulation of $\mathbf{X}$ on $\mathcal{M}$,

$$E_{field}(\mathbf{X}) = \sum_{i=1}^{n} \sum_{j \in \mathcal{N}(i)} w_{ij} \cdot D_{ij}, \quad (2)$$

where $\mathcal{N}(i)$ denotes the neighbor points of $\mathbf{x}_i$ and w_{ij} is the weight of edge e_{ij}, which will be discussed later.

Next, we give a detailed derivation of the direction distance *D* and discuss its properties in the case of 6-RoSy field. Given a sample point $\mathbf{x}_i$ and its neighbor point $\mathbf{x}_j$, $e_{ij} = \mathbf{x}_j - \mathbf{x}_i$ is the direction vector of the edge between $\mathbf{x}_i$ and $\mathbf{x}_j$, n_i is the unit normal vector and d_i is the unit vector representing the *N*-RoSy field, i.e. one of the *N* field vectors at $\mathbf{x}_i$.

Given n_i and d_i, a local coordinate system is established by a tuple of standard unit vectors $\{d_i, n_i \times d_i, n_i\}$. The directional angles θ and φ of edge e_{ij} is then defined in the common way used in spherical system, as shown in Fig. 3 (middle). Now, the direction sameness of edge e_{ij} and local field d_i can simply be measured by their inner product:

$$d_i^T \left(\frac{e_{ij}}{\|e_{ij}\|} \right) = (1,0,0) \cdot (\sin\theta\cos\varphi, \sin\theta\sin\varphi, \cos\theta)^T$$
$$= \sin\theta\cos\varphi.$$

To accord with the symmetry of *N*-RoSy field, we multiply φ with the symmetry number *N*, giving the *N*-RoSy direction sameness *S*,

$$S(e_{ij}, n_i, d_i) = \sin\theta\cos(N\varphi).$$

S is a $\frac{2\pi}{N}$ period function of φ, and is thus not affected by the choice of d_i. To get the *N*-RoSy direction distance, we first map $\cos(N\varphi)$ linearly to $[0, 1]$, which at the same time maps *S* to $[0, 1]$. Then, we calculate the difference between 1 and the image of *S*. The *N*-RoSy direction distance *D* is

$$D(e_{ij}, n_i, d_i) = 1 - \left(\frac{1 + \cos(N\varphi)}{2} \right) \sin\theta, \quad D \in [0,1] \quad (3)$$

To get an intuition of the field alignment term, let us take a close look at the 6-RoSy direction distance,

$$D_6 = 1 - \left(\frac{1 + \cos 6\varphi}{2} \right) \sin\theta.$$

Fig. 3 (right) visualizes D_6 on the surface of unit sphere. It is clear to see that this direction distance penalizes deviation from the local field and correctly represents the rotational symmetry. Fig. 3 (left) illustrates D_6 on the equatorial plane $\left(\theta = \frac{\pi}{2}\right)$. It is evident that the direction distance is 0 when the edge coincides with one of the
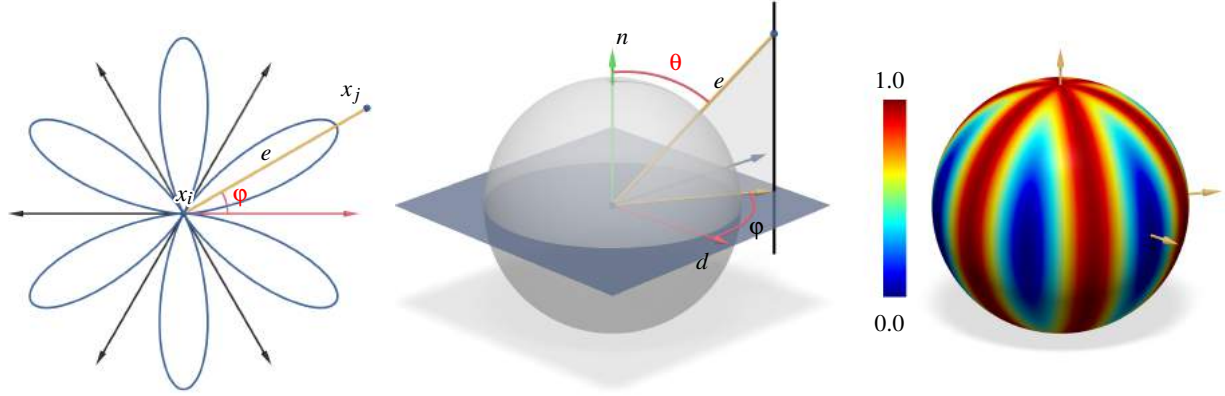
Figure 3: *Left: Illustration of 6-RoSy direction distance in 2D plane. Middle: Local coordinate system at a sample point is formed with local unit normal n and the representing field vector d. Edge e's direction angles is defined in the local coordinate system. Right: Visualization of 6-RoSy direction distance D_6 on a unit sphere. The distance penalizes deviation from local field and restrict edges on the tangent plane.*

field directions, and gets larger when the edge deviates from the field. Furthermore, this distance also serves to restrict mesh edges to be on the local tangent plane, as D_6 will increase if θ deviates from $\frac{\pi}{2}$.

3.5. Edge weight

The edge weight is used to ameliorate the smoothness of our field alignment term. To choose a proper weight for each edge, we consider the moment when an edge flips, as shown in Fig. 4. With a constant edge weight (e.g. $w = 1$), the total energy will change abruptly during the edge flip, making it difficult to optimize. In order to make the energy smoother, we assign very small weights to those edges that are prone to flip. In Delaunay triangulation, an edge flips when its two incident triangles share a common circumcircle. Viewed from the dual perspective, the corresponding Voronoi edge disappears when the primal triangle edge flips. Thus, the length of dual edge gives a suitable weight for the primal edge.
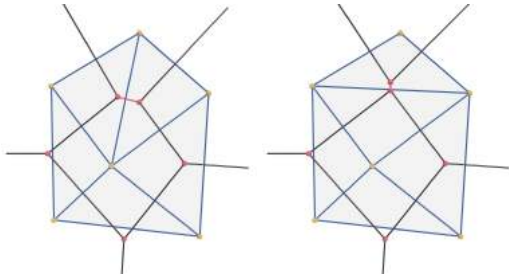

Figure 4: *Delaunay triangulation and its dual Voronoi diagram when an edge flips.*

4. Implementation Details

In this section, we present the implementation details of our field-aligned isotropic remeshing framework. The main building blocks include the field initialization, interpolation, and the energy minimization.

4.1. Direction field initialization

We use the direction field generation proposed in [JTPS15], which takes a mesh $\mathcal{M}$ as input and outputs the normal and field directions for each vertex of $\mathcal{M}$. Both normal and field directions are represented by unit 3D vectors. For triangle remeshing, a 6-RoSy field is used.

4.2. Direction field interpolation

To calculate the field alignment energy term for each sample point, the normal and field directions at the point are required. However, the generated field is only defined on vertices of the input mesh. Thus, it is necessary to interpolate the field direction over the entire mesh surface.

Direction interpolation over surface is a hard problem, especially for N-RoSy field. For 6-RoSy field, at each vertex, any one of the six direction vectors can be chosen to represent the field direction. Therefore, an elementary requirement for the interpolation method is that the output direction is not affected by the choice of field representation. Besides, to facilitate energy optimization, a smooth interpolation is desired, which is not addressed in [JTPS15].

Here we propose a novel interpolation scheme that interpolates normal and field directions over the mesh surface. We follow the piecewise paradigm, so that the interpolation result in a mesh triangle is determined by the direction information at its three vertices.

Fig. 5 shows the interpolation at point X in $\triangle ABC$. First, the normal direction is calculated as a weighted average of the normal directions of the three vertices.

$$n = w_A n_A + w_B n_B + w_C n_C$$

Here, we use the well-known discrete harmonic weights, as suggested in [HJ16b]. Then we normalize the normal direction to unit length. Given normal direction n, the field direction is restricted to be orthogonal to n. We shall find the direction d that has the least angle deviation from the field directions at the three vertices. For-
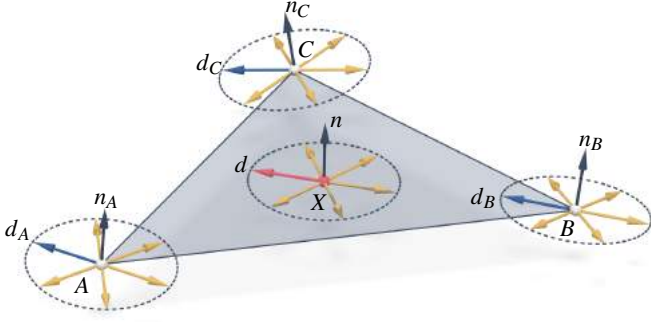
Figure 5: *Illustration of normal and field direction interpolation in △ABC.*

mally, d is determined as the maximizer of the following energy:

$$
\begin{aligned}
E_{\text{interpolation}} &= w_A d_A^T d + w_B d_B^T d + w_C d_C^T d \\
&= (w_A d_A + w_B d_B + w_C d_C)^T d \\
&= d_w^T d,
\end{aligned}
$$

where d_w denotes the weighted average of field directions, which can be decomposed into two components, one orthogonal to normal vector n, and the other parallel to n:

$$
d_w = nn^T d_w + (I - nn^T) d_w.
$$

Thus, the energy becomes

$$
\begin{aligned}
E_{\text{interpolation}} &= d_w^T d \\
&= d_w^T nn^T d + d_w^T (I - nn^T) d \\
&= d_w^T (I - nn^T) d.
\end{aligned}
$$

It is obvious that the energy is maximized when d has the same direction with $(I - nn^T) d_w$, and the maximal energy is $\|(I - nn^T) d_w\|$. To eliminate the influence of the choice of representation vectors at three vertices, we traverse all combinations of representation vectors to find the combination that maximizes $\|(I - nn^T) d_w\|$, thus also optimizes energy $E_{\text{interpolation}}$. Meanwhile, interpolated field direction d is set to be length-normalized $(I - nn^T) d_w$ produced by this combination of representation vectors.

Our method shares the spirit of extrinsic field smoothness with [HJ16b], since the difference between two directions is measured directly in 3D space. The result of interpolation is not affected by the choice of representation vectors. With a proper choice of weight, the smoothness is also guaranteed. Our interpolation method is simple and can be easily generalized to arbitrary N-RoSy field.

4.3. Energy minimization

We use a quasi-Newton solver (e.g., L-BFGS [LWL*09]) to minimize the proposed energy function, where the functional gradient w.r.t. points $\mathbf{X}$ is required. The gradient is composed of two parts, i.e., E_{CVT} and E_{field}, resp.

$$
\frac{\partial E_{tot}}{\partial \mathbf{X}} = \frac{\partial E_{CVT}}{\partial \mathbf{X}} + \lambda \frac{\partial E_{field}}{\partial \mathbf{X}}.
$$

Here $\frac{\partial E_{CVT}}{\partial \mathbf{x}_i} = 2m_i(\mathbf{x}_i - \mathbf{x}_i^*)$ [DFG99], where m_i is the mass of the restricted Voronoi cell $\Omega_{i|\mathcal{M}}$, and $\mathbf{x}_i^*$ is the restricted centroid [YLL*09].

For E_{field}, the partial derivative with respect to a sample point $\mathbf{x}_i$ is

$$
\frac{\partial E_{field}}{\partial \mathbf{x}_i} = \sum_{j \in \mathcal{N}(i)} \left(w_{ij} \cdot \frac{\partial D_{ij}}{\partial \mathbf{x}_i} + w_{ji} \cdot \frac{\partial D_{ji}}{\partial \mathbf{x}_i} \right)
$$

where $\mathcal{N}(i)$ denotes the neighbors of $\mathbf{x}_i$, w_{ij}, w_{ji} are edge weights and D is the direction distance function. The detailed calculation of the gradient of D is given in Appendix.
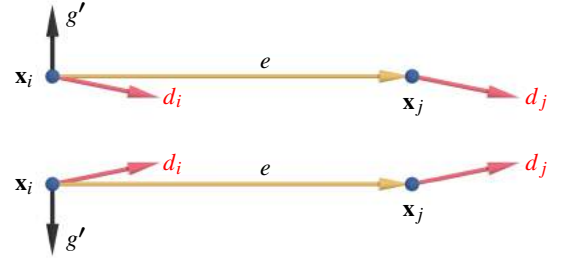

Figure 6: *Illustration of opposite gradient direction of field alignment energy in two different constant fields.*

To demonstrate the effectiveness of our field alignment term, we analyze the energy gradient in the simple case of 6-RoSy field in 2D plane, where θ is always $\pi/2$. In the following discussion, we assume a Cartesian coordinate system with standard unit vectors $\{e_x, e_y, e_z\}$, in which e_x and e_y lie in the 2D plane, and e_z is the normal direction. The partial derivative of the field alignment term of edge e with respect to $\mathbf{x}_i$ is

$$
\frac{\partial E_e}{\partial x_i} = 3(\sin 6(\varphi_e - \delta_i) + \sin 6(\varphi_e - \delta_j)) \cdot \frac{e \times e_z}{\|e\|^2}
$$

where φ_e is the directional angle of edge e, δ_i and δ_j are the angles of field direction at $\mathbf{x}_i$ and $\mathbf{x}_j$ respectively. These angles are relative to e_x.

Figure 6 shows an edge in two different constant fields. In both cases, we can see that the opposite gradient direction g' is the right moving direction for $\mathbf{x}_i$ to align the edge with the field.

4.4. Valence optimization

After energy optimization, we optimize vertex valence by minimizing the following mesh irregularity energy function:

$$
R = \sum_{v \in V} (d(v) - o(v))^2,
$$

where $d(v)$ is the valence of v and $o(v)$ is the optimal valence of v, usually set as 6 for inner vertices and 4 for boundary vertices.

Similar to previous approaches [BK04, DVBB13], we use three topology operators, edge flip, edge collapse and vertex split to minimize the energy function. For each irregular vertex, we find the topology operation that decreases the irregularity energy most. In each iteration, we select and apply those operations that decrease the irregularity most. After each topology operation, we use a local
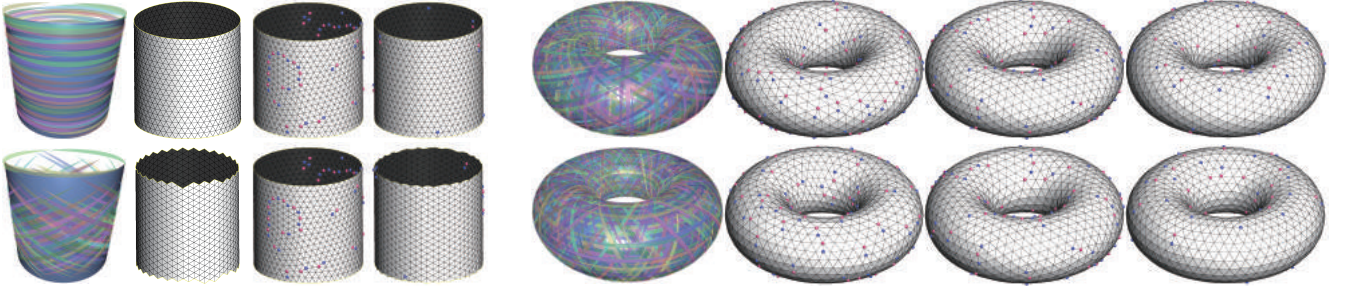
Figure 7: *Applying our approach on a cylinder and a torus model, whose maximal (top) and minimal (bottom) curvature directions are used as the vector field, resp. For each example, from left to right are the the vector fields, results of IFM, results of CVT, and our results.*

tangential smoothing step to repair the distortion induced by the operation. After the valence optimization, several FCVT iterations are performed to re-align mesh edges from possible deviation caused by valence optimization.

5. Experimental Results

We present our experiments in this section. We use the open-source library 'Geogram' [geo] for CVT computation, and 'Instant Meshes' program [JTPS15] for vector filed generation. All examples shown in this paper are produced on a PC with 4.00Ghz CPU, 16G RAM, under Win10 operating system. In the following, we first analyze the performance and the convergence behavior of our algorithm, FCVT. Then we give the detailed analysis of each parameter involved in our method. Finally, we evaluate and compare our results with the representative state-of-the-art remeshing techniques.

Convergence & performance We first verify the effectiveness of our algorithm on two specific input models, i.e., a cylinder and a torus, whose vector fields are manually chosen to be one of the principal curvature directions. As shown in Fig. 7, our method can capture the field information accurately, even for those special inputs. Our results contain very few singular vertices, which cannot be completely eliminated due to the global nature of the mesh connectivity. We compare our results with those of IFM. For the cylinder model, IFM can generate singular-free results because of the open-boundary condition, while ours contain a few singularities, which can be simply removed by pushing them to the boundary. For the torus model, our method gives better results with fewer singularities. In both tests, our method exhibits similar field alignment property to IFM and preserves the advantage of good mesh quality of CVT method (see Table 2).

Next, we analyze the convergence behavior of the proposed energy function. We apply our algorithm to three representative models and observe the convergence behavior of the CVT energy and field align energy, respectively. To eliminate the influence of input models size and the number of target sample points, we scale input models so that the average area per sample point is constant (namely, 1), and track the average energy per sample point during the process. We first apply pure CVT optimization to acquire a uniform sample distribution. Then, the field align term is enforced to improve edge orientation. Fig. 8 shows our experimental result. The Torus model has about 4k faces and 1k samples points, while both the Botijo and Bunny models have about 80k faces and 3k samples

points. Both pure CVT and FCVT optimization converge in about one hundred iteration steps. Moreover, the resulting average energy per sample points is nearly a constant, regardless of input models and the number of samples points. This verifies the stability of our method to various inputs.
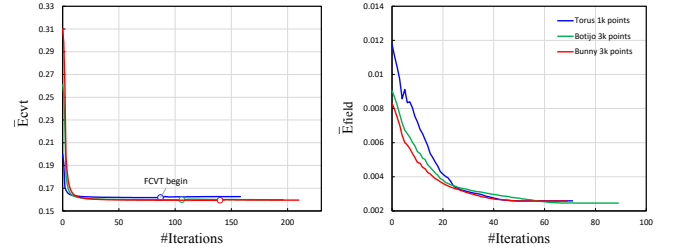

Figure 8: *Energy analysis. FCVT is performed after pure CVT convergence for three models, Torus(4k faces), Botijo(82k faces) and Bunny(72k faces). Both CVT and FCVT converges in about one hundred iterations and the converged average energy per sample point is nearly constant for all models. FCVT optimization also keeps CVT energy at a low level.*

Since our approach is based on energy minimization, the performance is not as efficient as IFM, which is based on the vector field tracing. Our algorithm is slightly slower than standard CVT algorithm [YLL*09] due to the extra gradient and energy evaluation of the field align term. However, since the most time-consuming part of the CVT framework is the RVD computation, which has a parallel version of the implementation on multi-core CPUs [geo], our algorithm is pretty fast and comparable to other approaches running on a multi-core CPU.

Uneven initial sampling. In our experiments, points are uniformly sampled over the input surface with respect to the density function for initialization. However, our method is also capable of handling uneven initialization. In such case, we first run Lloyd iteration several times to get a better initialization, then switch to the optimization process as described in Sec. 3. We test CVT and our method on a cylinder model with random and uneven initial sampling. Fig. 9 shows the results. Note that we do not claim it to be a contribution of our work, since this is the standard way to deal with uneven sampling.

Influence of λ. As discussed above, all the input models are scaled so that the average area per restricted Voronoi cell is a constant,
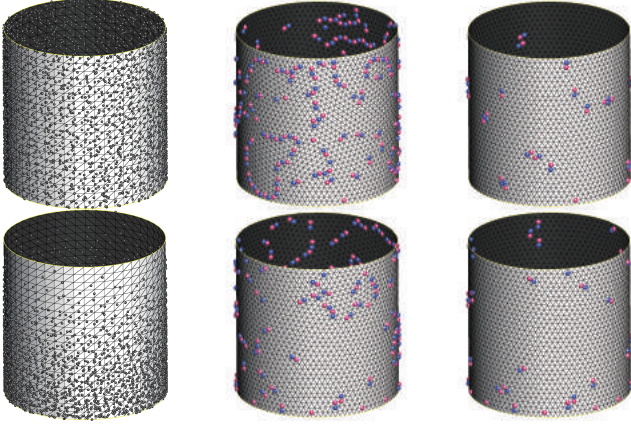
Figure 9: *Illustration of the influence of uneven initial sampling.*

which helps to normalize the parameter λ. Then, we test various choices of λ for different models and resolutions. The overall observation is that a smaller λ results in better triangle quality but more singular vertices, a larger λ reduces the number of singular points but scarifies the mesh quality. Fig. 10 shows the influence on valence and average triangle quality of varying λ on different models.
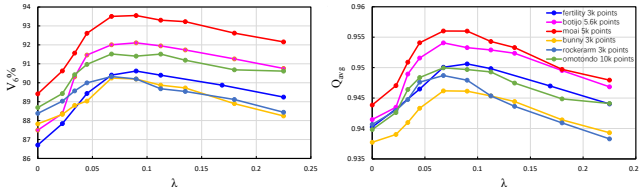

Figure 10: *Illustration of the influence of* λ.

Valence optimization. To validate the effectiveness of valence optimization, we compare remeshing results with and without valence optimization on the Botijo model. Three methods (CVT, FCVT and IFM) are used to remesh the model. Table 1 shows the result. For all methods, the rate of regular vertices increases after valence optimization, affirming the effectiveness of our valence optimization. In contrast, other metrics like average quality are relatively insensitive. The reason might be that the regular area already takes a major part of the mesh before valence optimization, making the improvement by valence optimization less remarkable. The experiments also show that FCVT is superior to CVT in average quality and regular rate even without valence optimization.

method	Q_{avg}	θ_{min}	$V_6\%$
CVT	0.94	40.3	86.9
CVT_Valence	0.94	39.4	90.7
OUR	0.95	37.8	92.4
OUR_Valence	0.95	37.5	93.7
IFM	0.96	17.7	93.0
IFM_Valence	0.96	19.8	94.5

Table 1: *Influence of valence optimization.*

Influence of resolution. We also test the performance of our algorithm under different target mesh resolution, i.e., different numbers of sample points. The experiment is carried on a torus model with 1.8k vertices. For various target resolution, we perform CVT, FCVT and IFM, and compare the quality of output meshes. To keep the comparison clear, we only focus on the energy minimization stage, and omit the valence optimization step. For each resolution, the experiment is repeated five times. Fig. 11 illustrates the experiment results.

We measure two groups of mesh qualities, namely, average qualities and extreme qualities. The average qualities includes the average triangle quality Q_{avg}, the average minimal angle $\bar{\theta}_{min}$, the percentage of the valence-6 vertices $V_6\%$, which represent mesh quality in an average sense. While extreme qualities, such as Q_{min}, θ_{min}, θ_{max} focus on extreme values and quality bound. In our experiments, we found that the average qualities generally benefit from field alignment, and this effect is further enhanced by increasing the output resolution, as can be seen from the first row of Fig. 11. In contrast, extreme qualities are less affected by resolution and only deteriorate slightly with increasing resolution, as illustrated by the second row of Fig. 11. On the other hand, CVT has an evident advantage over IFM in these extreme qualities, which is also preserved by our FCVT.
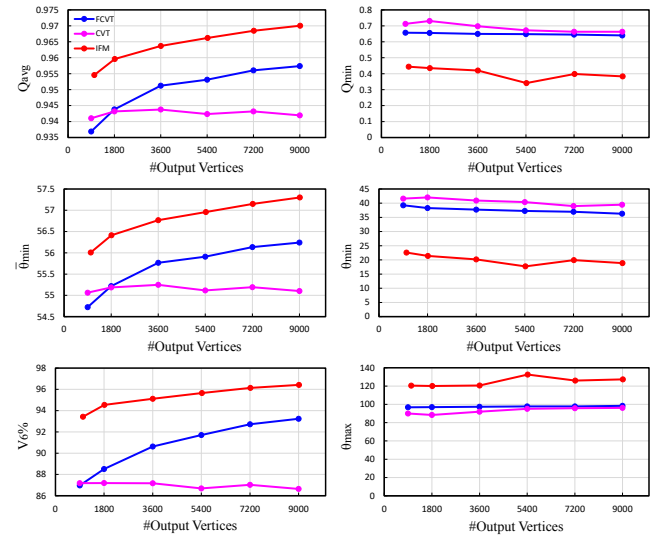
Figure 11: *Influence of output resolution on mesh quality. The experiment is performed on a torus model with 1.8k vertices. The left column shows FCVT and IFM have improved mesh qualities with denser output resolution. The right column shows that FCVT has preserved the advantage of CVT over IFM on some mesh qualities.*

From the comparison, we observe that for extreme mesh qualities, FCVT inherits the advantage of CVT. In addition, the field alignment ability of FCVT enables improvement of average qualities and a similar positive response to output resolution like IFM. Another interesting observation is that the critical resolution where FCVT outperforms CVT in average qualities is around 1.8k, i.e., the resolution of the input model. This is related to the piecewise harmonic field interpolation scheme used by FCVT. More specifically, the piecewise harmonic interpolation may lead to smoother

| [Field] | [MPS] | [RAR] | [CVT] | [IFM] | [OUR] |

Figure 12: *Comparison of uniform sampling results. From top to bottom are the results of Botijo, Bunny, Omotondo and Rockerarm. From left to right are the visualization of direction fields, remeshing results of MPS [YW13], RAR [DVBB13], CVT [YLL*09], IFM [JTPS15] and ours. The quality comparison is given in Table 2.*
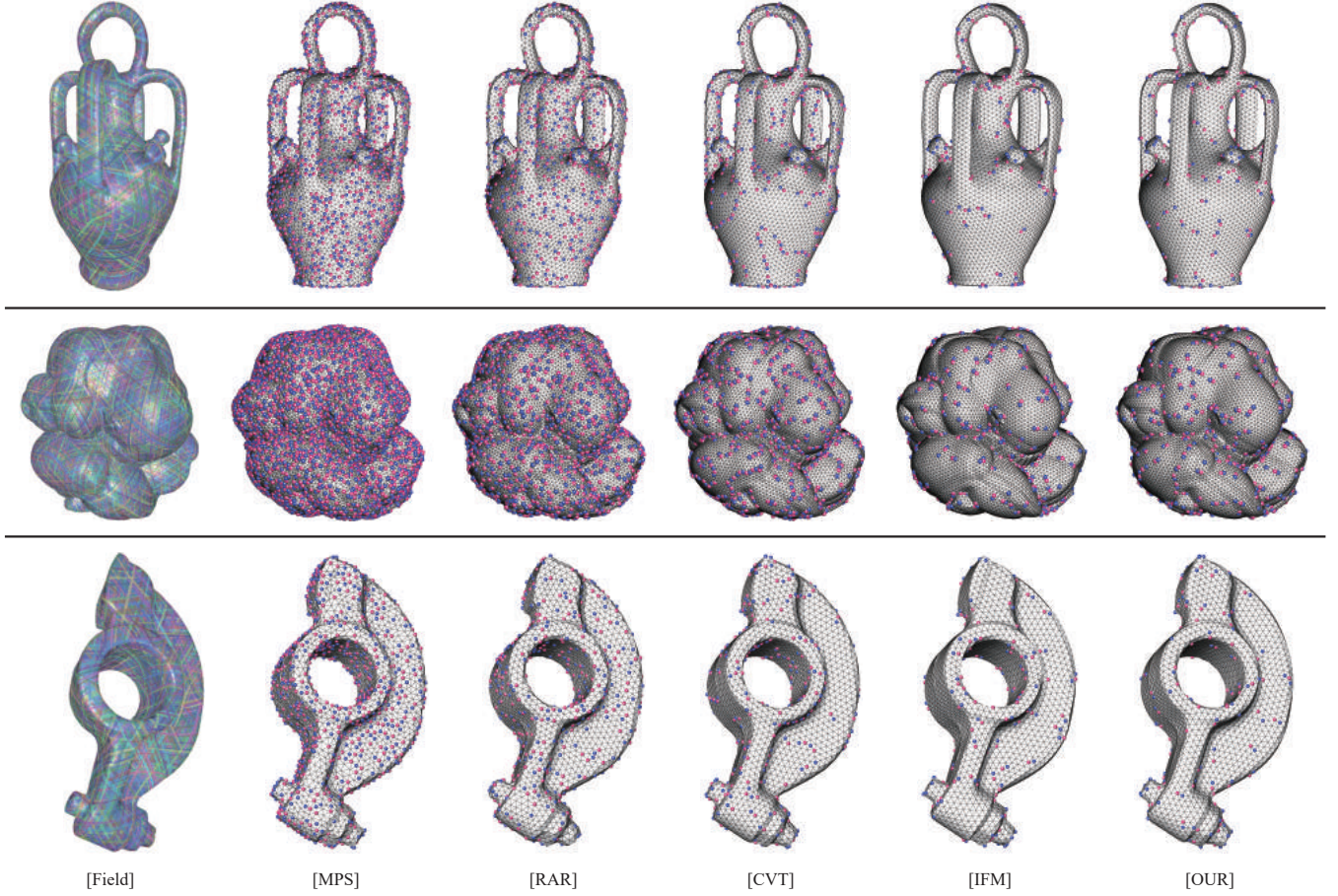
field in the interior of a triangle than at the common edge of two adjacent triangles. With increasing resolution, more pairs of adjacent sample points share a same input triangle, rather than residing on different triangles, thus improving overall energy smoothness and resulting in meshes with better quality. The results in the top row of Fig. 11 also validate the effectiveness of our field interpolation algorithm. According to [JTPS15], IFM requires the input mesh to have higher resolution than the output, otherwise the input mesh has to be further subdivided. The results here imply that our interpolated field is comparable with the field produced by the "subdivide and optimize" process of IFM.

Sharp feature handling. Our method is also able to handle input meshes with sharp features. The features on the input mesh are either detected automatically by some algorithms or manually selected by the user. Similar to [YLL*09], a two-stage strategy is used to preserve sharp features. In the first stage, sample points are optimized freely to obtain an optimal distribution. In the second stage, each sample point whose restricted Voronoi cell intersects with a feature line is snapped onto the line and confined on the feature in the following optimization. Fig. 14 shows several results of our method applied to models with sharp features.

Comparison. We first compare our approach with the most related approaches, i.e., CVT and IFM, in terms of visual effect and mesh quality. Our results are obtained by first applying 65 CVT iterations and then 65 FCVT iterations. The results of CVT are obtained by applying 130 CVT iterations (or less if converged earlier). The visual effect (Fig. 1, 7, 12, and 13) shows that our results are well aligned to the underlying vector fields, which are able to capture the anisotropic features as well as produce well-shaped triangle. Moreover, the singular point distribution of our approach is quite similar to that of IFM. We further compare our method with IFM [JTPS15] on adaptive remeshing in Fig. 13. Due to the global nature of IFM, it is difficult to adapt the edge length locally, which results in large distortion in regions with highly changing density. Fig. 15 shows another example that uses a density function with large gradation.

Next, we compare our results with several representative state-of-the-art approaches, including *Maximal Poisson-disk Sampling* (MPS) [YW13], *Realtime Adaptive Remeshing* (RAR) based on local connectivity optimization [DVBB13]. We use the standard mesh quality evaluation metric for comparison. The quality of a triangle is measured by $Q(t) = \frac{2\sqrt{3}|t|}{p_t h_t}$, where $|t|$ is the area of triangle t, p_t the inscribed radius of t and h_t the length of the longest
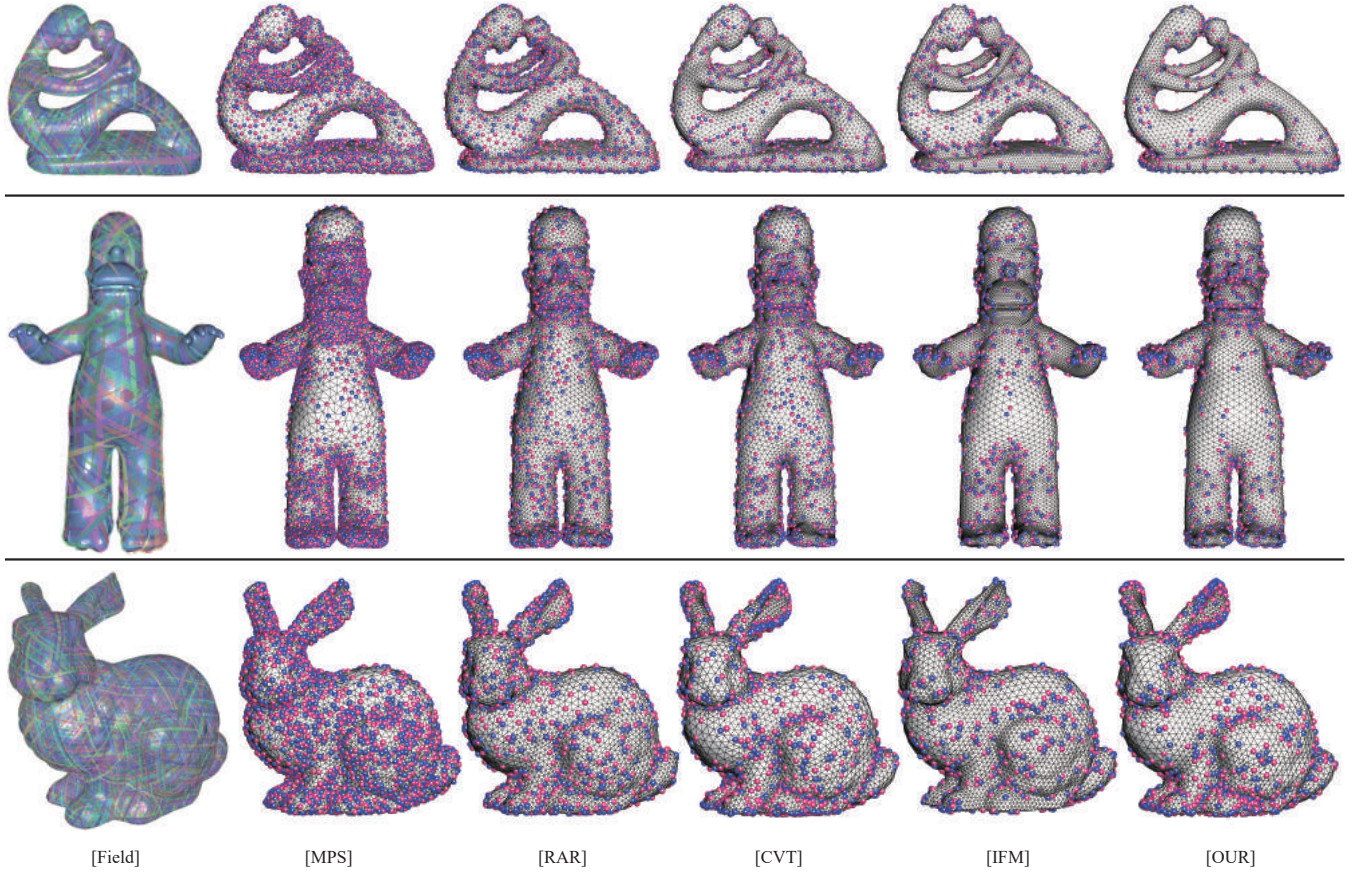
Figure 13: *Comparison of adaptive sampling results. From left to right are the visualization of direction fields, remeshing results of MPS [Y-W13], RAR [DVBB13], CVT [YLL*09], IFM [JTPS15] and ours. The quality comparison is given in Table 2.*
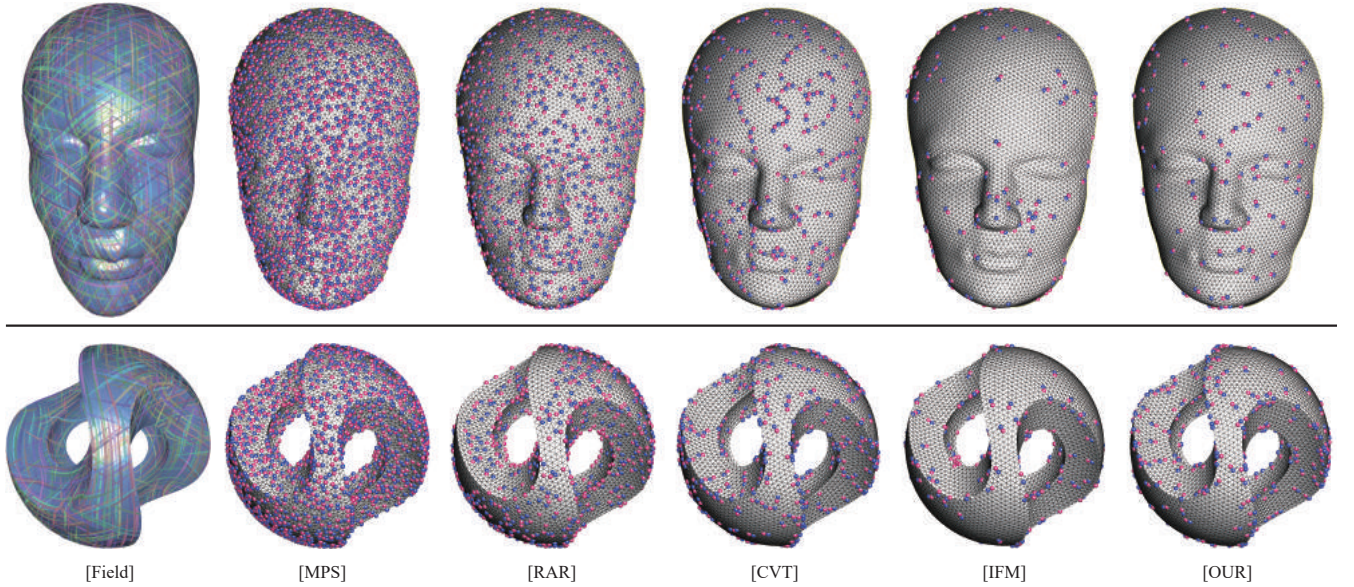

Figure 14: *Results of feature preservation.*

edge of t. An equilateral triangle has $Q(t) = 1$ and a degenerate triangle has $Q(t) = 0$ [FB97]. Table 2 lists the numerical statistics of all the approaches we compare against. In addition to the quality measured in Fig. 11, we also count the percentage of the triangles with small and large angles, e.g., $\theta_{min} < 30°$ and $\theta_{max} > 90°$, which reflect the overall triangle quality distribution of each method. Finally, we measure the Hausdroff distance and the root mean square error between the remesh and the input mesh. From these quantitive comparison, we further validate that our approach preserves both the advantages of isotropic remeshing and field remeshing. For example, our results always have better θ_{min} than IFM, and better regularity than MPS, RAR, and CVT.
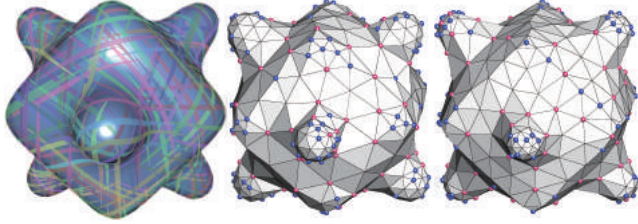

Figure 15: *Comparison of adaptive remeshing with IFM. Both IFM and our method are able to generate meshes with large triangle area contrast. However, our result better aligns to the underlying shape and is less distorted compared to the result of IFM.*

Limitation. There are some limitations of our current approach. First, in the adaptive sampling scenario, the remeshing result is not as good as that of CVT, since the density function always conflicts with the field alignment constraint. Another limitation is that the field interpolation is somehow time-consuming, during which we have to project each sample back onto the surface, and transverse all combinations of representation vectors. We plan to improve upon these problems in our future work.

6. Conclusion and Future Work

We present a novel approach that combines the CVT-based isotropic remeshing with vector field alignment. Different from other approaches that modify the distance metrics [LL10, SCW*11], we impose the filed alignment as a penalty term added to the standard CVT energy function, which results in a much simpler implementation. We demonstrate that our results exhibit both advantages of isotropic and field-aligned remeshing, i.e., fewer singularities and higher mesh qualities. In the future, we plan to try to use the field defined on facets instead of on vertices, which can improve the performance. Another interesting problem is to find the correspondence between singularities of the input field and singularities of the resulting mesh. We would also like to further exploit the potential power of our approach by apply it to potential applications.

Acknowledgements

References

[ACSD*03] ALLIEZ P., COHEN-STEINER D., DEVILLERS O., LÉVY B., DESBRUN M.: Anisotropic polygonal remeshing. *ACM Trans. on Graphics (Proc. SIGGRAPH) 22*, 3 (2003), 485–493. 2

[AGY*17] AHMED* A., GUO* J., YAN D.-M., FRANCESCHI J.-Y., ZHANG X., DEUSSEN O.: A simple push-pull algorithm for blue-noise sampling. *IEEE Trans. on Vis. and Comp. Graphics* (2017). accepted. 2

[AMD02] ALLIEZ P., MEYER M., DESBRUN M.: Interactive Geometry Remeshing. *ACM Trans. on Graphics (Proc. SIGGRAPH) 21(3)* (2002), 347–354. 2

[AUGA08] ALLIEZ P., UCELLI G., GOTSMAN C., ATTENE M.: Recent advances in remeshing of surfaces. In *Shape Analysis and Structuring* (2008), pp. 53–82. 2

[AVDI03] ALLIEZ P., VERDIÉRE É. C. D., DEVILLERS O., ISENBURG M.: Isotropic surface remeshing. In *Shape Modeling International - SMI* (2003), pp. 49–58. 2

[BK04] BOTSCH M., KOBBELT L.: A remeshing approach to multiresolution modeling. In *Proc. of Symp. of Geometry Processing* (2004), pp. 189–196. 2, 5

[BKP*10] BOTSCH M., KOBBELT L., PAULY M., ALLIEZ P., LÉVY B.: *Polygon Mesh Processing*. AK Peters, 2010. 2

[BLP*13] BOMMES D., LÉVY B., PIETRONI N., PUPPO E., SILVA C. T., TARINI M., ZORIN D.: Quad-mesh generation and processing: A survey. *Computer Graphics Forum 32*, 6 (2013), 51–76. 2

[Boi05] BOISSONNAT J.-D. O. S.: Provably good sampling and meshing of surfaces. *Graphical Models 67* (2005), 405Í451. 2

[BSTY15] BOISSONNAT J., SHI K., TOURNOIS J., YVINEC M.: Anisotropic delaunay meshes of surfaces. *ACM Trans. on Graphics 34*, 2 (2015), 14:1–14:11. 2

[BW10] BRONSON JONATHAN R.AND LEVINE J. A., WHITAKER R. T.: *Particle Systems for Adaptive, Isotropic Meshing of CAD Models*. 2010, pp. 279–296. 2

[CCW12] CHEN Z., CAO J., WANG: W.: Isotropic surface remeshing using constrained centroidal delaunay mesh. *Computer Graphics Forum 31*, 7-1 (2012), 2077–2085. 2

[CDS12] CHENG S.-W., DEY T. K., SHEWCHUK J. R.: *Delaunay Mesh Generation*. CRC Press, 2012. 2

[Che93] CHEW L. P.: Guaranteed-quality mesh generation for curved surfaces. In *Proceedings of the Ninth Symposium on Computational Geometry* (1993), pp. 274–280. 2

[Che04] CHEN L.: Mesh smoothing schemes based on optimal delaunay triangulations. p. 109Í120. 2

[DFG99] DU Q., FABER V., GUNZBURGER M.: Centroidal Voronoi tessellations: applications and algorithms. *SIAM Review 41* (1999), 637–676. 2, 5

[dGDT16] DE GOES F., DESBRUN M., TONG Y.: Vector field processing on triangle meshes. In *ACM SIGGRAPH 2016 Courses* (2016), SIGGRAPH '16, pp. 27:1–27:49. 3

[DKG05] DONG S., KIRCHER S., GARLAND M.: Harmonic functions for quadrilateral remeshing of arbitrary manifolds. *Comp. Aided Geom. Design 22*, 5 (2005), 392 – 423. 2

[DVBB13] DUNYACH M., VANDERHAEGHE D., BARTHE L., BOTSCH M.: Adaptive remeshing for real-time mesh deformation. In *Eurographics Short Papers Proceedings* (2013), pp. 29–32. 1, 2, 5, 8, 9

[ERA*16] EBEIDA M., RUSHDI A. A., AWAD M. A., MAHMOUD A. H., YAN D.-M., ENGLISH S. A., OWENS J. D., BAJAJ C. L., MITCHELL S. A.: Disk density tuning of a maximal random packing. *Computer Graphics Forum (Proc. SGP)* (2016). 2

[FB97] FREY P. J., BOROUCHAKI H.: Surface mesh evaluation. In *IMR* (1997), pp. 363–374. 10

Model	Method	$\|\mathbf{X}\|$	$\|t\|$	Q_{min}	Q_{avg}	θ_{min}	$\bar{\theta}_{min}$	θ_{max}	$\theta_{<30^o}\%$	$\theta_{>90^o}\%$	$V_6\%$	$d_{RMS}(\times 10^{-3})$	$d_H(\times 10^{-2})$	*Timing(s)*
Cylinder	CVT	1K	2K	0.74	0.96	42.1	56.4	87.8	**0**	**0**	81.60	2.73	1.64	2.14
	IFM	1K	2K	**1.00**	**1.00**	**59.7**	**59.9**	**60.4**	**0**	**0**	**90.00**	**0.90**	**0.87**	**0.04**
	IFM_CF	1K	2K	0.99	0.99	58.9	59.3	60.8	**0**	**0**	88.22	0.94	1.87	0.05
	OUR	1K	2K	0.70	0.98	41.6	57.7	91.9	**0**	0.05	88.32	2.74	1.60	2.98
	OUR_CF	1K	2K	0.64	0.96	38.3	56.5	98.1	**0**	0.21	86.45	2.89	2.14	2.49
Torus	CVT	1K	2K	**0.72**	**0.94**	**42.9**	54.7	**89.2**	**0**	**0**	85.39	1.21	0.27	2.13
	IFM	1K	2K	0.42	0.87	21.2	49.4	124.4	1.21	5.34	82.78	**0.43**	**0.22**	**0.07**
	IFM_CF	1K	2K	0.36	0.88	17.6	50.5	126.2	1.25	4.36	83.55	**0.43**	0.25	**0.07**
	OUR	1K	2K	0.65	**0.94**	39.1	54.6	98.0	**0**	0.60	89.78	1.24	0.29	2.66
	OUR_CF	1K	2K	0.64	0.93	39.0	54.1	98.4	**0**	0.55	**90.80**	1.25	0.30	2.84
Moai	MPS	5K	10K	0.58	0.82	32.0	46.2	104.9	**0**	12.62	55.64	0.85	0.83	2.19
	RAR	5K	10K	**0.67**	0.92	35.3	52.7	**94.6**	**0**	**0.05**	75.93	0.78	0.96	1.07
	CVT	5K	10K	0.66	0.94	31.4	54.8	96.0	**0**	0.06	85.96	0.80	**0.57**	15.15
	IFM	5K	10K	0.34	**0.96**	16.4	**56.3**	130.5	0.33	1.20	**94.29**	**0.60**	0.71	**0.80**
	OUR	5K	10K	0.64	0.95	**36.9**	56.0	98.7	**0**	0.31	93.94	0.81	0.65	21.66
Botijo	MPS	5.6K	11K	0.52	0.83	31.7	47.0	113.2	**0**	9.49	56.28	0.64	0.73	1.48
	RAR	5.6K	11K	**0.67**	0.91	36.1	52.3	**94.1**	**0**	0.06	74.15	0.66	1.06	1.05
	CVT	5.6K	11K	0.66	0.94	**39.7**	54.8	96.3	**0**	**0.03**	86.11	0.71	0.45	13.18
	IFM	5.6K	11K	0.31	**0.96**	18.0	**56.2**	139.1	0.35	1.25	**93.26**	**0.39**	0.46	**0.64**
	OUR	5.6K	11K	0.65	0.95	37.0	55.9	97.1	**0**	0.21	92.99	0.72	**0.44**	19.41
Omotondo	MPS	10K	20K	0.49	0.82	30.2	45.9	117.1	**0**	13.31	54.56	0.78	0.59	5.42
	RAR	10K	20K	0.66	0.91	36.5	52.5	**95.6**	**0**	**0.04**	75.80	0.79	0.90	2.38
	CVT	10K	20K	0.58	0.94	35.5	54.7	106.1	**0**	0.13	85.64	0.58	0.45	33.81
	IFM	10K	20K	0.41	**0.96**	19.3	**56.1**	119.3	0.34	1.24	**94.28**	**0.33**	0.39	**1.43**
	OUR	10K	20K	**0.66**	0.95	**39.3**	55.7	96.5	**0**	0.08	93.07	0.58	0.41	46.00
Rockerarm	MPS	3K	6K	0.58	0.82	32.1	46.4	104.9	**0**	11.89	54.09	1.23	0.86	1.34
	RAR	3K	6K	**0.67**	0.91	36.1	52.6	**92.8**	**0**	0.03	75.88	1.05	1.12	0.59
	CVT	3K	6K	**0.67**	0.94	**41.1**	54.8	96.0	**0**	**0.02**	85.93	1.12	0.65	10.47
	IFM	3K	6K	0.41	**0.95**	18.0	55.4	122.6	0.47	1.69	91.00	**0.65**	**0.59**	**0.60**
	OUR	3K	6K	0.64	**0.95**	37.3	**55.5**	98.3	**0**	0.40	**91.97**	1.14	0.67	13.69
Fertility	MPS	7K	14K	0.61	0.83	32.1	46.6	100.0	**0**	10.47	55.98	0.42	0.35	3.19
	RAR	7K	14K	0.47	0.89	23.1	50.4	116.7	0.16	1.51	75.78	**0.29**	**0.25**	**1.38**
	CVT	7K	14K	**0.63**	**0.93**	**35.6**	53.8	**99.7**	**0**	**0.24**	83.70	0.70	2.32	8.11
	IFM	7K	14K	0.54	**0.93**	32.2	**54.1**	110.9	**0**	0.58	82.96	0.36	0.27	3.38
	OUR	7K	14K	0.54	**0.93**	30.0	53.6	109.5	**0**	2.05	**88.41**	0.71	0.41	18.99
Homer	MPS	10K	20K	0.58	0.82	32.0	46.2	105.0	**0**	12.17	54.78	0.35	0.34	2.88
	RAR	10K	20K	**0.59**	0.90	28.4	51.3	101.4	**0**	0.31	76.81	**0.22**	0.21	**2.63**
	CVT	10K	20K	**0.59**	0.92	27.8	53.2	**100.9**	0.02	0.54	79.59	0.34	0.76	9.18
	IFM	10K	20K	0.55	**0.94**	35.0	54.8	109.2	**0**	0.18	**88.02**	0.26	0.26	3.85
	OUR	10K	20K	0.49	0.92	24.1	52.7	116.1	0.13	2.68	86.89	0.37	**0.20**	22.26
Bunny	MPS	5K	10K	0.39	0.80	20.1	45.0	125.8	0.91	15.39	47.53	0.66	0.54	4.27
	RAR	5K	10K	0.44	0.90	**27.9**	51.1	123.4	0.04	**0.90**	**74.99**	**0.52**	0.48	**1.05**
	CVT	5K	10K	**0.49**	0.89	23.4	50.5	115.6	0.30	2.12	70.85	0.87	0.35	13.09
	IFM	5K	10K	**0.49**	**0.91**	26.9	**52.2**	117.2	**0.08**	2.01	70.93	0.76	0.47	2.55
	OUR	5K	10K	**0.49**	0.89	21.5	50.7	**113.3**	0.42	2.75	71.61	0.86	**0.33**	24.44
Mask	MPS	4K	8K	0.49	0.81	30.5	45.3	116.4	**0**	15.06	47.34	0.38	0.45	1.64
	RAR	4K	8K	0.35	0.91	13.1	52.2	119.3	0.06	0.47	73.29	0.33	0.47	**0.39**
	CVT	4K	8K	0.63	0.95	36.0	55.5	98.9	**0**	**0.10**	84.80	0.38	0.34	3.19
	IFM	4K	8K	0.43	**0.96**	21.3	**56.6**	122.3	0.44	1.16	**91.58**	**0.28**	0.70	0.89
	OUR	4K	8K	**0.68**	**0.96**	**40.3**	56.5	**94.4**	**0**	**0.10**	91.02	0.38	**0.33**	6.86
Sculpt	MPS	6K	12K	0.49	0.81	**30.2**	45.2	116.4	**0**	15.75	49.31	0.21	0.64	3.48
	RAR	6K	12K	0.48	0.90	23.7	51.4	112.4	0.01	**0.30**	77.55	**0.16**	**0.06**	**0.59**
	CVT	6K	12K	0.55	0.93	26.4	53.8	105.5	0.05	1.22	84.70	0.22	0.07	6.50
	IFM	6K	12K	0.42	**0.96**	19.0	**56.0**	124.0	0.45	1.49	**93.52**	0.22	0.60	1.25
	OUR	6K	12K	**0.57**	0.94	25.9	54.7	**103.4**	0.07	1.35	88.77	0.22	0.07	11.02

Table 2: *Comparison of remeshing quality with previous techniques. The best result of each measurement is marked in* **bold** *font.* $\|\mathbf{X}\|$ *is the number of vertices;* $\|t\|$ *is the number of triangles. The other measurements are explained in Sec. 5.*

[FLSG14] FU X., LIU Y., SNYDER J., GUO B.: Anisotropic simplicial meshing using local convex functions. *ACM Trans. on Graphics (Proc. SIGGRAPH Asia) 33*, 6 (2014), 182:1–182:11. 2

[FZ08] FU Y., ZHOU B.: Direct sampling on surfaces for high quality remeshing. In *ACM symposium on Solid and physical modeling* (2008), pp. 115–124. 2

[geo] GEOGRAM. https://gforge.inria.fr/projects/geogram/. 6

[GYJZ15] GUO J., YAN D.-M., JIA X., ZHANG X.: Efficient maximal Poisson-disk sampling and remeshing on surfaces. *Computers & Graphics 46*, 6-8 (2015), 72–79. 2

[HDD∗93] HOPPE H., DEROSE T., DUCHAMP T., MCDONALD J., STUETZLE W.: Mesh optimization. In *Proc. ACM SIGGRAPH* (1993), pp. 19–26. 2

[HJ16a] HUANG Z., JU T.: Extrinsically smooth direction fields. *Computers & Graphics 58* (2016), 109–117. 3

[HJ16b] HUANG Z., JU T.: Extrinsically smooth direction fields. *Comput. Graph. 58*, C (Aug. 2016), 109–117. 4, 5

[HYB∗17] HU K., YAN D.-M., BOMMES D., ALLIEZ P., BENES B.: Error-bounded and feature preserving surface remeshing with minimal angle improvement. *IEEE Trans. on Vis. and Comp. Graphics* (2017). 2

[HZP∗11] HUANG J., ZHANG M., PEI W., HUA W., BAO H.: Controllable highly regular triangulation. *SCIENCE CHINA Information Sciences 54*, 6 (2011), 1172–1183. 2

[JTPS15] JAKOB W., TARINI M., PANOZZO D., SORKINE-HORNUNG O.: Instant field-aligned meshes. *ACM Trans. on Graphics (Proc. SIGGRAPH Asia) 34*, 6 (2015), 189:1–189:15. 1, 2, 3, 4, 6, 8, 9, 10

[LB12] LÉVY B., BONNEEL N.: Variational anisotropic surface meshing with Voronoi parallel linear enumeration. In *Proceedings of the 21st International Meshing Roundtable* (2012), pp. 349–366. 2

[LJX∗10] LAI Y., JIN M., XIE X., HE Y., PALACIOS J., ZHANG E., HU S., GU X.: Metric-driven RoSy field design and remeshing. *IEEE Trans. on Vis. and Comp. Graphics 16*, 1 (2010), 95–108. 2

[LL10] LÉVY B., LIU Y.: L_p centroidal Voronoi tesselation and its applications. *ACM Trans. on Graphics (Proc. SIGGRAPH) 29*, 4 (2010), 119:1–11. 2, 10

[LWL∗09] LIU Y., WANG W., LÉVY B., SUN F., YAN D.-M., LU L., YANG C.: On centroidal Voronoi tessellation - energy smoothness and fast computation. *ACM Trans. on Graphics 28*, 4 (2009), 101:1–101:11. 5

[LXW∗11] LIU Y., XU W., WANG J., ZHU L., GUO B., CHEN F., WANG G.: General planar quadrilateral mesh design using conjugate direction field. *ACM Trans. on Graphics (Proc. SIGGRAPH Asia) 30*, 6 (2011), 140:1–140:10. 2

[LXY∗16] LIU Y.-J., XU C.-X., YI R., FAN D., HE Y.: Manifold differential evolution (mde): A global optimization method for geodesic centroidal voronoi tessellations on meshes. 243:1–11. 2

[Mey07] MEYER M.D. K. R. W. R.: Topology, accuracy, and quality of isosurface meshes using dynamic particles. *IEEE Trans. on Vis. and Comp. Graphics 13*, 6 (2007), 1704ĺC1711. 2

[NPPZ11] NIESER M., PALACIOS J., POLTHIER K., ZHANG E.: Hexagonal global parameterization of arbitrary surfaces. *IEEE Trans. on Vis. and Comp. Graphics 18*, 6 (2011), 865–878. 2

[Ren15] RENKA R. J.: Two simple methods for improving a triangle mesh surface. *Computer Graphics Forum* (2015), to appear. 2

[SCW∗11] SUN F., CHOI Y.-K., WANG W., YAN D.-M., LIU Y., LÉVY B.: Obtuse triangle suppression in anisotropic meshes. *Comp. Aided Geom. Design 28*, 9 (2011), 537–548. 10

[SSG03] SIFRI O., SHEFFER A., GOTSMAN C.: Geodesic-based surface remeshing. In *Proceedings of the 12th International Meshing Roundtable, IMR 2003* (2003), pp. 189–199. 2

[Tur92] TURK G.: Re-tiling polygonal surfaces. In *Proc. ACM SIGGRAPH* (1992), pp. 55–64. 2

[VCD∗16] VAXMAN A., CAMPEN M., DIAMANTI O., BOMMES D., HILDEBRANDT K., BEN-CHEN M., PANOZZO D.: Directional field synthesis, design, and processing. In *SIGGRAPH ASIA 2016 Courses* (2016), SA '16, pp. 15:1–15:30. 3

[VCP08] VALETTE S., CHASSERY J.-M., PROST R.: Generic remeshing of 3D triangular meshes with metric-dependent discrete Voronoi diagrams. *IEEE Trans. on Vis. and Comp. Graphics 14*, 2 (2008), 369–381. 2

[WYL∗15] WANG X., YING X., LIU Y.-J., XIN S.-Q., WANG W., GU X., MUELLER-WITTIG W., HE Y.: Intrinsic computation of centroidal Voronoi tessellation (CVT) on meshes. *Computer-Aided Design 58*, 0 (2015), 51 – 61. 2

[YBZW14] YAN D.-M., BAO G., ZHANG X., WONKA P.: Low-resolution remeshing using the localized restricted Voronoi diagram. *IEEE Trans. on Vis. and Comp. Graphics 20*, 10 (2014), 418–1427. 2

[YLL∗09] YAN D.-M., LÉVY B., LIU Y., SUN F., WANG W.: Isotropic remeshing with fast and exact computation of restricted Voronoi diagram. *Computer Graphics Forum (Proc. SGP) 28*, 5 (2009), 1445–1454. 1, 2, 3, 5, 6, 8, 9

[YW13] YAN D.-M., WONKA P.: Gap processing for adaptive maximal Poisson-disk sampling. *ACM Trans. on Graphics 32*, 5 (2013), 148:1–148:15. 1, 2, 8, 9

[YW16] YAN D., WONKA P.: Non-obtuse Remeshing with Centroidal Voronoi Tessellation. *IEEE Trans. on Vis. and Comp. Graphics 22*, 9 (2016), 2136–2144. 2

[ZGW∗13] ZHONG Z., GUO X., WANG W., LÉVY B., SUN F., LIU Y., MAO W.: Particle-based anisotropic surface meshing. *ACM Trans. on Graphics (Proc. SIGGRAPH) 32*, 4 (2013), 99:1–99:14. 2

[Zha16] ZHANG E.: Course notes rotational symmetries on surfaces: Theory, algorithms, and applications. In *SIGGRAPH ASIA 2016 Courses* (2016), SA '16, pp. 10:1–10:13. 3

Appendix: Partial derivatives of field alignment energy

In this appendix, we derive the closed-from partial derivative of the field alignment energy function, which is required by quasi-Newton optimization methods. Since 2D planar mesh can be regarded as a special case of surface mesh, we focus on the field alignment energy of 3D surface mesh.

Given a sample point $\mathbf{x}_i$ and its neighbor point $\mathbf{x}_j$, and the edge e connecting the two points. The contribution of edge e to the total field alignment energy comes from its two opposite direction $e_{ij} = \mathbf{x}_j - \mathbf{x}_i$ and $e_{ji} = -e_{ij}$,

$$
\begin{aligned}
E_e &= E_{ij} + E_{ji} \\
&= w_{ij} \cdot D_{ij} + w_{ji} \cdot D_{ji} \\
&= w_{ij} \cdot D(e_{ij}, n_i, d_i) + w_{ji} \cdot D(e_{ji}, n_j, d_j)
\end{aligned}
$$

where w_{ij} and w_{ji} are edge weights, n_i, n_j, d_i, d_j are normal and field vectors at the two points, and D is the direction distance function.

Viewing the edge weights as constant, the partial derivative of E_e with respect to point $\mathbf{x}_i$ is

$$
\frac{\partial E_e}{\partial \mathbf{x}_i} = w_{ij} \frac{\partial D(e_{ij}, n_i, d_i)}{\partial \mathbf{x}_i} + w_{ji} \frac{\partial D(e_{ji}, n_j, d_j)}{\partial \mathbf{x}_i}
$$

The direction distance functions are

$$
D(e_{ij}, n_i, d_i) = 1 - \left(\frac{1 + \cos(N\varphi_{ij})}{2} \right) \sin\theta_{ij}
$$

$$
D(e_{ji}, n_j, d_j) = 1 - \left(\frac{1 + \cos(N\varphi_{ji})}{2} \right) \sin\theta_{ji}
$$

where N is the rotation symmetry number of the field, $(\|e_{ij}\|, \theta_{ij}, \varphi_{ij})$ are the spherical coordinates of $\mathbf{x}_j$ in local coordinate system at $\mathbf{x}_i$, and similarly $(\|e_{ji}\|, \theta_{ji}, \varphi_{ji})$ are spherical coordinates of $\mathbf{x}_i$ in local coordinate system at $\mathbf{x}_j$. The local coordinate system is illustrated in Fig. 3 (middle).

The partial derivetaves are

$$\frac{\partial D_{ij}}{\partial \mathbf{x}_i} = \frac{N \sin(N\varphi_{ij}) \sin\theta_{ij}}{2} \cdot \frac{\partial \varphi_{ij}}{\partial \mathbf{x}_i} - \left(\frac{1 + \cos(N\varphi_{ij})}{2}\right) \cos\theta_{ij} \frac{\partial \theta_{ij}}{\partial \mathbf{x}_i}$$

$$\frac{\partial D_{ji}}{\partial \mathbf{x}_i} = \frac{N \sin(N\varphi_{ji}) \sin\theta_{ji}}{2} \cdot \frac{\partial \varphi_{ji}}{\partial \mathbf{x}_i} - \left(\frac{1 + \cos(N\varphi_{ji})}{2}\right) \cos\theta_{ji} \frac{\partial \theta_{ji}}{\partial \mathbf{x}_i}$$

θ and φ are functions of the edge vector e and local coordinate system $\{d, n \times d, n\}$,

$$\theta = \Theta(e, n, d), \quad \varphi = \Phi(e, n, d)$$

Recall that in spherical coordinate system, the gradient is,

$$\nabla f = \frac{\partial f}{\partial r}\hat{\mathbf{r}} + \frac{1}{r}\frac{\partial f}{\partial \theta}\hat{\theta} + \frac{1}{r\sin\theta}\frac{\partial f}{\partial \varphi}\hat{\varphi}$$

where $\hat{\mathbf{r}}, \hat{\theta}, \hat{\varphi}$ are the local orthogonal unit vectors in the direction of increasing r, θ and φ.

so,

$$\nabla\theta = \frac{1}{r}\hat{\theta}, \quad \nabla\varphi = \frac{1}{r\sin\theta}\hat{\varphi}$$

Thus, the partial derivatives are

$$\frac{\partial \Theta}{\partial e} = \frac{1}{\|e\|}\hat{\theta}$$
$$= \frac{e \times (e \times n)}{\|e\|^2 \|e \times n\|}$$
$$\frac{\partial \Phi}{\partial e} = \frac{1}{\|e\|\sin\theta}\hat{\varphi}$$
$$= \frac{\hat{\mathbf{r}} \times \hat{\theta}}{\|e \times n\|}$$
$$= \frac{1}{\|e \times n\|}e \times \frac{\partial \Theta}{\partial e}$$
$$= -\frac{e \times n}{\|e \times n\|^2}$$

In the case of $\mathbf{x}_i$ and $\mathbf{x}_j$,

$$\theta_{ij} = \Theta(e_{ij}, n_i, d_i)$$
$$\varphi_{ij} = \Phi(e_{ij}, n_i, d_i)$$
$$\theta_{ji} = \Theta(e_{ji}, n_j, d_j)$$
$$\varphi_{ji} = \Phi(e_{ji}, n_j, d_j)$$

The partial derivatives with respect to $\mathbf{x}_i$ are

$$\frac{\partial \theta_{ij}}{\partial \mathbf{x}_i} = \frac{\partial \Theta}{\partial e_{ij}}\frac{\partial e_{ij}}{\partial \mathbf{x}_i} + \frac{\partial \Theta}{\partial n_i}\frac{\partial n_i}{\partial \mathbf{x}_i} + \frac{\partial \Theta}{\partial d_i}\frac{\partial d_i}{\partial \mathbf{x}_i}$$
$$= -\frac{\partial \Theta}{\partial e_{ij}} + \frac{\partial \Theta}{\partial n_i}\frac{\partial n_i}{\partial \mathbf{x}_i} + \frac{\partial \Theta}{\partial d_i}\frac{\partial d_i}{\partial \mathbf{x}_i}$$

$$\frac{\partial \varphi_{ij}}{\partial \mathbf{x}_i} = \frac{\partial \Phi}{\partial e_{ij}}\frac{\partial e_{ij}}{\partial \mathbf{x}_i} + \frac{\partial \Phi}{\partial n_i}\frac{\partial n_i}{\partial \mathbf{x}_i} + \frac{\partial \Phi}{\partial d_i}\frac{\partial d_i}{\partial \mathbf{x}_i}$$
$$= -\frac{\partial \Phi}{\partial e_{ij}} + \frac{\partial \Phi}{\partial n_i}\frac{\partial n_i}{\partial \mathbf{x}_i} + \frac{\partial \Phi}{\partial d_i}\frac{\partial d_i}{\partial \mathbf{x}_i}$$

$$\frac{\partial \theta_{ji}}{\partial \mathbf{x}_i} = \frac{\partial \Theta}{\partial e_{ji}}\frac{\partial e_{ji}}{\partial \mathbf{x}_i} + \frac{\partial \Theta}{\partial n_j}\frac{\partial n_j}{\partial \mathbf{x}_i} + \frac{\partial \Theta}{\partial d_j}\frac{\partial d_j}{\partial \mathbf{x}_i}$$
$$= \frac{\partial \Theta}{\partial e_{ji}}$$

$$\frac{\partial \varphi_{ji}}{\partial \mathbf{x}_i} = \frac{\partial \Phi}{\partial e_{ji}}\frac{\partial e_{ji}}{\partial \mathbf{x}_i} + \frac{\partial \Phi}{\partial n_j}\frac{\partial n_j}{\partial \mathbf{x}_i} + \frac{\partial \Phi}{\partial d_j}\frac{\partial d_j}{\partial \mathbf{x}_i}$$
$$= \frac{\partial \Phi}{\partial e_{ji}}$$

We assume that the local varience of the normal and field direction is tiny, thus

$$\frac{\partial n_i}{\partial \mathbf{x}_i} \approx 0, \quad \frac{\partial d_i}{\partial \mathbf{x}_i} \approx 0$$

In this condition, we get

$$\frac{\partial \theta_{ij}}{\partial \mathbf{x}_i} \approx -\frac{\partial \Theta(e_{ij}, n_i, d_i)}{\partial e_{ij}} = -\frac{e_{ij} \times (e_{ij} \times n_i)}{\|e_{ij}\|^2 \|e_{ij} \times n_i\|}$$
$$\frac{\partial \varphi_{ij}}{\partial \mathbf{x}_i} \approx -\frac{\partial \Phi(e_{ij}, n_i, d_i)}{\partial e_{ij}} = \frac{e_{ij} \times n_i}{\|e_{ij} \times n_i\|^2}$$
$$\frac{\partial \theta_{ji}}{\partial \mathbf{x}_i} = \frac{\partial \Theta(e_{ji}, n_j, d_j)}{\partial e_{ji}} = \frac{e_{ij} \times (e_{ij} \times n_j)}{\|e_{ij}\|^2 \|e_{ij} \times n_j\|}$$
$$\frac{\partial \varphi_{ji}}{\partial \mathbf{x}_i} = \frac{\partial \Phi(e_{ji}, n_j, d_j)}{\partial e_{ji}} = \frac{e_{ij} \times n_j}{\|e_{ij} \times n_j\|^2}$$

The total partial derivative of E_{field} with respect to point $\mathbf{x}_i$ is

$$\frac{\partial E_{field}}{\partial \mathbf{x}_i} = \sum_{j \in \mathcal{N}(i)} \left(w_{ij} \cdot \frac{\partial D_{ij}}{\partial \mathbf{x}_i} + w_{ji} \cdot \frac{\partial D_{ji}}{\partial \mathbf{x}_i}\right)$$